Atmospheric-pressure plasma transfer across dielectric channels and tubes

Zhongmin Xiong[1]**, Eric Robert**[2]**, Vanessa Sarron**[2]**, Jean-Michel Pouvesle**[2] **and Mark J Kushner**[1]

[1] Electrical Engineering and Computer Science Department, University of Michigan, Ann Arbor, MI 48109, USA
[2] GREMI, UMR7344, CNRS-Polytech'Orléans, 45067 Orléans Cedex 2, France

E-mail: zxiong@umich.edu, mjkush@umich.edu, eric.robert@univ-orleans.fr, vanessa.sarron@univ-orleans.fr and jean-michel.pouvesle@univ-orleans.fr

Abstract

Atmospheric-pressure plasma transfer refers to producing an ionization wave (IW) in a tube or channel by impingement of a separately produced IW onto its outer surface. In this paper, we report on numerical and experimental investigations of this plasma transfer phenomenon. The two tubes, source and transfer, are perpendicular to each other in ambient air with a 4 mm separation with both tubes being flushed with Ne or a Ne/Xe gas mixture at 1 atmosphere pressure. The primary IW is generated in the source tube by ns to μs pulses of ± 25 kV, while the transfer tube is electrodeless, not electrically connected to the first and at a floating potential. The simulations are conducted using a two-dimensional (2D) plasma hydrodynamics model with radiation transport, where the three-dimensional tubes in the experiments are represented by 2D channels. Simulations and experiments show that the primary IW propagates across the inter-tube gap and upon impingement induces two secondary IWs propagating in opposite directions in the transfer tube. Depending on the polarity of the primary IW in the source tube, the secondary IW in the transfer tube can have polarities either the same or opposite to that of the primary IW. The speed and strength of both the primary and secondary IWs depend on the rate of rise of the voltage pulse in the source tube. The modelling results were found to agree well with the behaviour of plasma transfer observed using nanosecond intensified charge-coupled device imaging.

(Some figures may appear in colour only in the online journal)

1. Introduction

Atmospheric-pressure ionization waves (IWs) generated by nanosecond, high-voltage pulses have recently attracted interest due to their emerging applications in plasma-assisted combustion, high-speed flow control, plasma-assisted film deposition, plasma sterilization and plasma medicine [1–7]. In particular, IWs confined within narrow dielectric tubes, rigid or flexible, are capable of travelling up to tens to hundreds of cm distance in the tube at speeds of 10^7–10^8 cm s^{-1}, and exiting the tube as a plasma jet [8–10]. The unique ability of IWs to generate and deliver active plasma species and the associated electric field and photon fluxes to remote locations via small diameter tubes opens up new potential applications, such as thin-film deposition on the inner surface of the tubes [3], plasma sterilization of catheters, and treating internal organs and body cavities by delivering cold plasmas through endoscopic devices [11–13].

The propagation and mutual interaction of plasma IWs through different type of capillary tubes and channels have been the subject of recent experimental and numerical studies [9, 14–17], with the goal of understanding the basic dynamics of confined IWs and developing the capability to regulate the IWs by, for example, redirecting IWs to different paths or adjusting their strengths. Beyond IWs propagating through the dielectric tubes in which they are produced, recent experiments have found that under certain conditions IWs can also propagate across dielectric barriers [17]. This phenomenon, called *plasma transfer*, here refers to an IW exiting from the source tube, impinging onto the outer surface
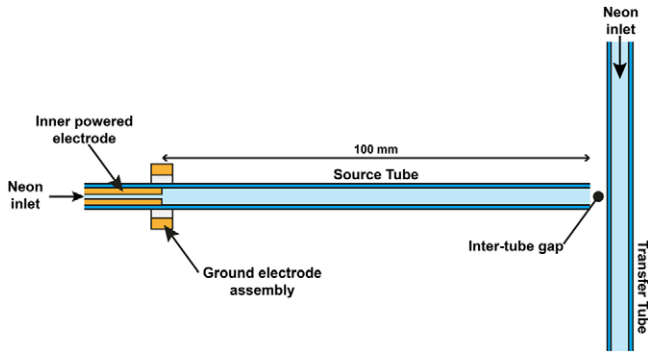
Figure 1. Experimental setup of atmospheric-pressure neon plasma transfer using a plasma gun. Both tubes are made of borosilicate glass with a 4 mm inner diameter and a 1 mm wall thickness. The tubes are flushed with neon and placed in ambient air with an inter-tube gap of 4 mm. The peak driving voltage is ±25 kV for microsecond pulse and −25 kV for nanosecond pulse.

of a spatially separate and electrodeless second tube, and producing a new IW inside the second tube [18–21]. (See, for example, figure 1.) The first tube and IW are the source tube and primary IW. The second tube and IW are the transfer tube and secondary IW. Visually, the IWs coming from the source tube appear to continue their propagation in the transfer tube by first crossing the inter-tube air gap and then penetrating the dielectric wall of the transfer tube. For example, in recent experiments using an atmospheric-pressure helium plasma jet, a dielectric barrier was inserted into the propagation path of the jet. Upon impingement the plasma bullet visually appears to penetrate the wall and continue its propagation [21]. These phenomena are well captured in simulations [17].

Based on these experiments, it is believed that the electric field induced by charge deposition from the primary IW on the intervening dielectric surface produces a sufficiently large electric field on the other side to launch the secondary IW. The details of the plasma transfer mechanism, however, remain unclear. In this paper, we report on a joint numerical and experimental investigation of plasma transfer between a primary IW launched from a cylindrical source jet to a cross-wise secondary IW in a cylindrical transfer tube. The source and transfer tubes are perpendicular to each other with a 4 mm separation in ambient air. The transfer tube is electrodeless, not electrically connected to the source tube and is at a floating potential. Both tubes are flushed with Ne during the experiments and with a gas mixture of Ne/Xe (99.9/0.1) at atmospheric pressure for modelling studies. The primary IW was generated in the source tube by voltage pulses of up to ±25 kV with rise times varying between 25–400 ns. The numerical simulations were conducted with a two-dimensional (2D) model where the three-dimensional (3D) tubes in the experiments were represented by 2D channels. Experimental diagnostics include plasmas emission using ns resolved intensified charge-coupled device (ICCD) imaging.

Simulations and experiments show that the primary IW propagates across the inter-tube gap and, upon impingement, induces two secondary IWs propagating in opposite directions in the transfer tube from the site of impingement of the primary IW. For primary IWs produced with positive voltage pulses,

the polarity of the secondary IW is also positive. For primary IWs produced with negative voltage pulses, the polarity of the secondary IWs is not negative but also positive—a polarity reversal occurs as a result of electron charge deposition on the outer surface of the transfer tube. The dynamics of the secondary IWs depends weakly on the amount of preionization in the transfer tube. The rate of rise (dV/dt) of the primary voltage pulse affects the speed and the strength of both the primary and secondary IWs. In the case of polarity reversal, there is threshold rise time beyond which the secondary IW cannot be produced in the transfer tube.

Brief descriptions of the experimental discharge configuration and the 2D modelling platform are given in section 2. Numerical results of the plasma transfer for positive and negative primary IWs are presented in section 3 along with the comparisons with experiments. Our discussion and concluding remarks are in section 4.

2. Description of the experiment and model

2.1. Description of the experiment

The schematic of the plasma transfer experimental setup is shown in figure 1. The plasma is triggered in a horizontal tube flushed with a 150 sccm (standard cubic centimetre per minute, 1 sccm = 4.478×10^{17} atoms s^{-1}) neon flow at atmospheric pressure. (The choice of neon instead of, for example, argon, was made for convenience. The bright red emission from neon is readily recorded by the ICCD system.) This 15 cm long horizontal tube, labelled as the source tube, is equipped with an outer grounded electrode and an inner hollowed powered electrode through which the neon flow is flushed. The distance between the inner electrode tip and the outlet of the source tube is 10 cm. The inner brass electrode is 50 mm long and has a hollowed channel 1 mm in diameter. The outer electrode is a 5 mm wide brass ring centred with the inner electrode tip. This part of the experimental apparatus represents the basic configuration of the plasma gun [9]. In this work, the plasma gun was first powered with a lab-developed pulsed high-voltage power supply delivering microsecond duration waveforms. The peak voltage was ±25 kV with a pulse repetition rate of 100 Hz. This is a sufficiently low repetition rate that all experiments can be considered *single shot*. In a second set of experiments, the plasma gun was powered with negative polarity, 25 kV peak amplitude waveforms having a nanosecond rise time and a microsecond long decay period, delivered at 100 Hz from a lab-developed power supply. Voltage measurements were performed with a Tektronix P6015A 75 MHz probe connected to a Tektronix 744 oscilloscope. Details of plasma gun operation and the waveforms of the voltage pulses with micro- and nanosecond rise times are discussed in [9].

For plasma transfer studies, a second 50 cm long tube, labelled as the transfer tube in figure 1, was set perpendicularly to the axis of the source tube with a gap of 4 mm between the outlet of the source tube and the outer wall of the transfer tube. The transfer tube is flushed with a 150 sccm neon flow at atmospheric pressure. Both tubes are made of borosilicate

glass with 4 mm inner diameter and 1 mm wall thickness. Neon (Air Liquide) with a 99.999% stated purity from the supplier was used. In the numerical model, the xenon admixture was added to mimic the gas impurities (H_2O, hydrocarbons, CO, CO_2, CF_4 and He) in the neon flow and the residual air impurities adsorbed on the inner tube surfaces and the powered electrode.

The ICCD images were captured using a PI-MAX3 Roper scientific camera, equipped with a 50 mm lens, and driven by a 10 ns duration gated pulse. No spectral filter was used during imaging experiment so that the plasma emission captured by the ICCD device mainly consists of the red neon lines excited in both tubes and in the inter-tube gap where a large neon fraction is preserved (as inferred from figure 2(*c*)). In the following, all the time delays at which the time-resolved microsecond and nanosecond images were captured refer to the same time origin, set at the voltage onset.

2.2. Description of the model

The 2D simulations of plasma transfer are performed using *nonPDPSIM*, a plasma hydrodynamics model with radiation transport [15, 16]. The model is the same as described in [16], and so will be briefly described. Based on a 2D unstructured finite volume discretization, *nonPDPSIM* solves the transport equations for all charged species and Poisson's equation for electric potential using a fully implicit Newton's method. Updates of the charged particle densities and electric potential are followed by an implicit update of the electron temperature, T_e, neutral particle densities, beam electron transport and neutral flow field properties. The use of the electron energy equation allows for non-equilibrium between the local electric field and the electron transport coefficients, which are obtained from stationary solutions of the Boltzmann equation. In the simulations reported, a gas mixture of Ne/Xe= 99.9/0.1 was used to fill both source and transfer tubes at atmospheric pressure and 300 K. The reaction mechanism is discussed in [16]. Due to the 2D nature of our simulation, the 3D dielectric tubes used in the experiments are approximated by 2D channels in the simulations.

The configuration of the plasma transfer used in the model is based on the experimental setup described above and is shown in figure 2 . The source (vertical) channel contains the initiating electrodes and the transfer (horizontal) channel is electrodeless and not electrically connected to the source channel. The lengths of the source and transfer channels were chosen to be 2.5 and 8.0 cm, respectively, which are shorter than those in the experiments, in order to save computation cost. These shorter lengths do not affect the final answer. The channel width and wall thickness for both channels (glass, $\varepsilon_r = 4$) are 4 mm and 1 mm. The 4 mm inter-channel gap is the same as in the experiments. The full computational domain (not shown) is a $15 \times 12\,cm^2$ rectangular region filled with ambient air with all the boundaries grounded. This separation between the source and transfer channels divides the plasma domain into two discrete zones, separated by the upper wall of the transfer channel. The first zone consists of the interior of the source channel and the (shaped) inter-gap region,
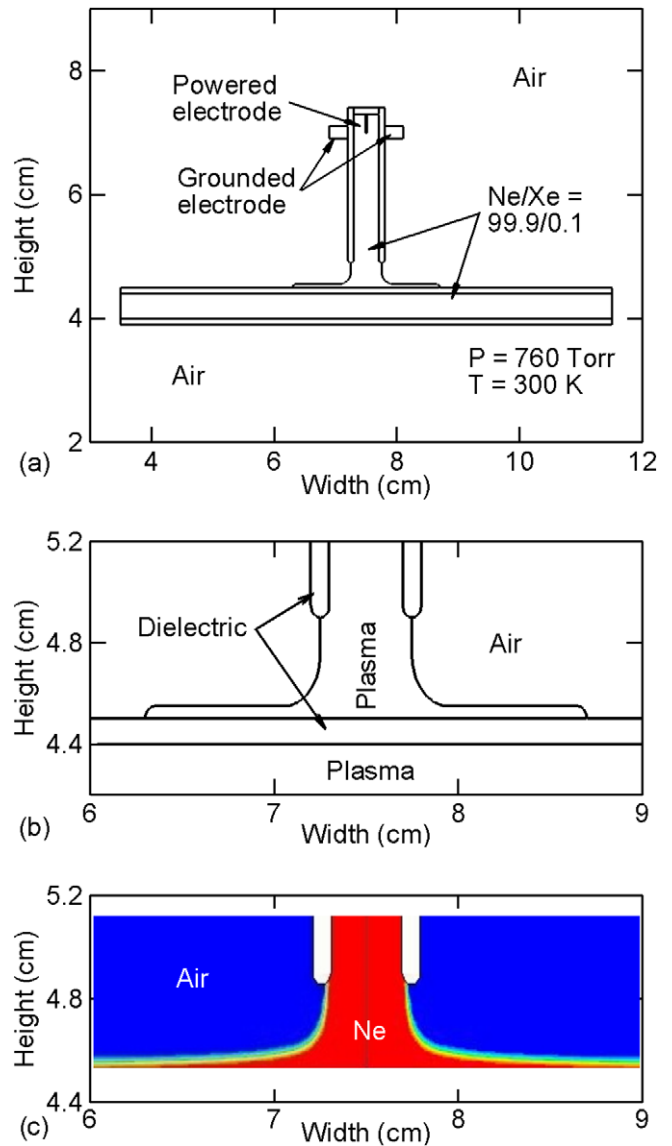

Figure 2. Plasma transfer configuration in the model between a source (vertical) and a transfer (horizontal) dielectric channel placed in ambient air with a 4 mm inter-channel gap. (*a*) Both channels are filled with Ne/Xe = 99.9/0.1 at one atmosphere pressure. The IW is initiated by a voltage pulse applied to the needle powered electrode. The full computational domain is a 15×12 cm rectangle whose boundaries are grounded. (*b*) The enlarged inter-gap plasma region. (*c*) Mole fractions of neon (red) and air (blue) of an axisymmetric impinging neon jet, computed using Ansys Fluent v12.1.

while the second zone occupies the interior of the transfer channel.

The propagation of IWs through rare gas jets into air typically has a limited extent. As the jet extends into the air, air diffuses into the jet, diluting the rare gas. When the air mole fraction exceeds a critical value, the IWs terminate. For example, experiments have shown that IWs in a helium plasma jet emerging into ambient air can only propagate through that portion of the jet where the mole fraction of the helium exceeds 0.3–0.5 [22, 23]. To take advantage of these observations and so simplify the model, the following procedure was followed.

The mixing between neon and air was numerically simulated using the commercial computational fluid dynamics (CFD) software Ansys Fluent v.12 for the geometry shown in figure 2. The specific gas flow conditions are as follows. A circular jet of pure neon was issued from a vertical tube (4 mm inner diameter and 1 mm wall thickness) into ambient air and impinged upon a flat horizontal wall placed 4 mm downstream at atmospheric pressure and room temperature. The mean velocity of the pure neon at the tube entrance is $20\,\mathrm{cm\,s^{-1}}$, corresponding to 150 sccm. A no-slip boundary condition was applied on all the solid walls. The jet mixing flow was assumed to be incompressible, steady state and laminar. Strictly speaking, the outer surface of the transfer tube is not flat and hence the flow in the experiments is 3D. However, for simplicity, the curvature of the transfer tube at the stagnation point was neglected, and the flow is thus assumed to be axisymmetric. The computed mole fraction distribution of the neon–air mixture in the inter-gap region is shown in figure 2(*c*).

As shown in figure 2(*b*), the plasma transport equations are solved inside both the source and transfer channels and in a transition region between the channels that is surrounded by ambient air. This region consists of a straight, extruded portion from the exit of the source channel extending to the transfer channel, and a lateral portion which spreads on the top surface of the transfer channel. The shape the Ne/Xe filled plasma zone and the boundary with air are determined by the contour line of 30% mole fraction of neon obtained from the CFD calculation. The surrounding air was then treated simply as dielectric having relative permittivity $\varepsilon_\mathrm{r} = 1$. The plasma zone spreading on the top outer surface of the transfer channel is 0.5 mm thick and 24 mm in length. The total number of nodes in the resulting numerical mesh is about 14 000, of which about 8000 are distributed in the two plasma zones. The computational mesh was also refined around the powered electrode, in the inter-channel gap and close to the upper wall of the transfer channel, with the mesh size varying between $20\,\mu\mathrm{m}$ and $100\,\mu\mathrm{m}$.

The primary IW was initiated at the inlet of the source channel between a pair of grounded electrodes outside the channel and a needle-like, powered electrode inside the channel. The length and width of the needle are 0.3 and 0.02 cm, and the radius of curvature at the needle tip is 0.01 cm. A 25 kV voltage pulse with either positive or negative polarity was applied to the powered electrode with a rise time ranging from 25 ns to $0.4\,\mu\mathrm{s}$. After rising to its peak ($\pm25\,\mathrm{kV}$), the voltage is held constant for 50 ns, followed by a falling period (decreasing to zero) equal to the rise time. The initial electron density inside the source and transfer channels is zero except for two small electrically neutral plasma clouds on the centre lines of each channel. In the source channel, the cloud is at the tip of the powered electrode, has a radius of $250\,\mu\mathrm{m}$ and peak value of $[e] \approx 10^{10}\,\mathrm{cm^{-3}}$. Inside the transfer channel, the cloud is at the intersection point of the axes of the two channels. It has an elliptical shape with the major (horizontal) and minor (vertical) radius of 2.5 mm and 0.5 mm and peak value of $[e] \approx 10^8\,\mathrm{cm^{-3}}$ in the base case. (This value was varied with the results discussed below.) The magnitude of the initial plasma cloud for the base case in the transfer tube was chosen so that the secondary IWs can be ignited by the primary IW with either positive or negative polarity. Once ignited, however, the dynamics of the secondary IWs, as will be discussed below, is nearly independent to the preionization electron density.

3. Dynamics of plasma transfer

3.1. Plasma emission

The dynamic processes of the plasma transfer for a positive primary IW are shown in figure 3(*a*) by a series of time-resolved ICCD images having ns exposure times. Time-integrated plasma emission when the primary IW crosses the air gap and intersects the transfer tube is shown in figure 3(*b*). The emission is a view from the top. The outlines of the source and transfer tubes are shown as dotted lines. The primary IW is driven by a microsecond voltage pulse of Gaussian form with 25 kV peak magnitude and $\approx4\,\mu\mathrm{s}$ FWHM. The corresponding images for a negative primary IW are shown in figure 4(*a*). Images for the negative primary IW driven by a nanosecond voltage pulse ($-25\,\mathrm{kV}$ peak amplitude, $\approx50\,\mathrm{ns}$ rising front and $1\,\mu\mathrm{s}$ duration decay) are shown in figure 4(*b*). The sub-images in each sequence were obtained from separate discharge pulses, and so there is some pulse-to-pulse jitter in the timing. For example, in figure 3(*a*), the last image (2540 ns) had a particularly long delay in starting (larger jitter).

For the positive polarity shown in figure 3, the IW propagates through the source tube, crosses the gap between the tubes much like a plasma bullet and impinges on the outer wall of the transfer tube. Immediately after the primary IW impinges on the transfer tube wall, two secondary IWs form inside the transfer tube directly beneath where the primary IW impinges. The IW is likely circular or oval but appears to be two IWs when viewed from the top. The two newly formed secondary IWs continue to propagate in the same direction as the primary IW, crossing the diameter of the transfer tube and impinging upon the opposite inner wall. The dynamics of the primary IW apparently penetrating the dielectric wall and producing two secondary IWs in a sealed transfer tube does not seem to significantly differ from the splitting of an IW front when it enters a T-junction formed by two *connected* tubes. In the latter case, IWs cross the junction as streamers and intersect the opposite surface. Similar to the connected tubes, when the secondary IWs intersect the opposite wall in the transfer tube, two independent IWs are launched in opposite directions. This results from charging of the opposite wall, which produces lateral components of the electric field which then support the IWs.

The primary IW appears to propagate in a wall-hugging mode until it reaches the end of the source tube. The IW then becomes centred on the axis of the source tube crossing the gap, intersects and spreads on the top of transfer tube, presumably charging this surface positively. The stronger emission in the transfer tube is concentrated near the upper inner wall, and at the edges of the plasma region, where the two new, side-going secondary IW fronts form. Some filaments of emission
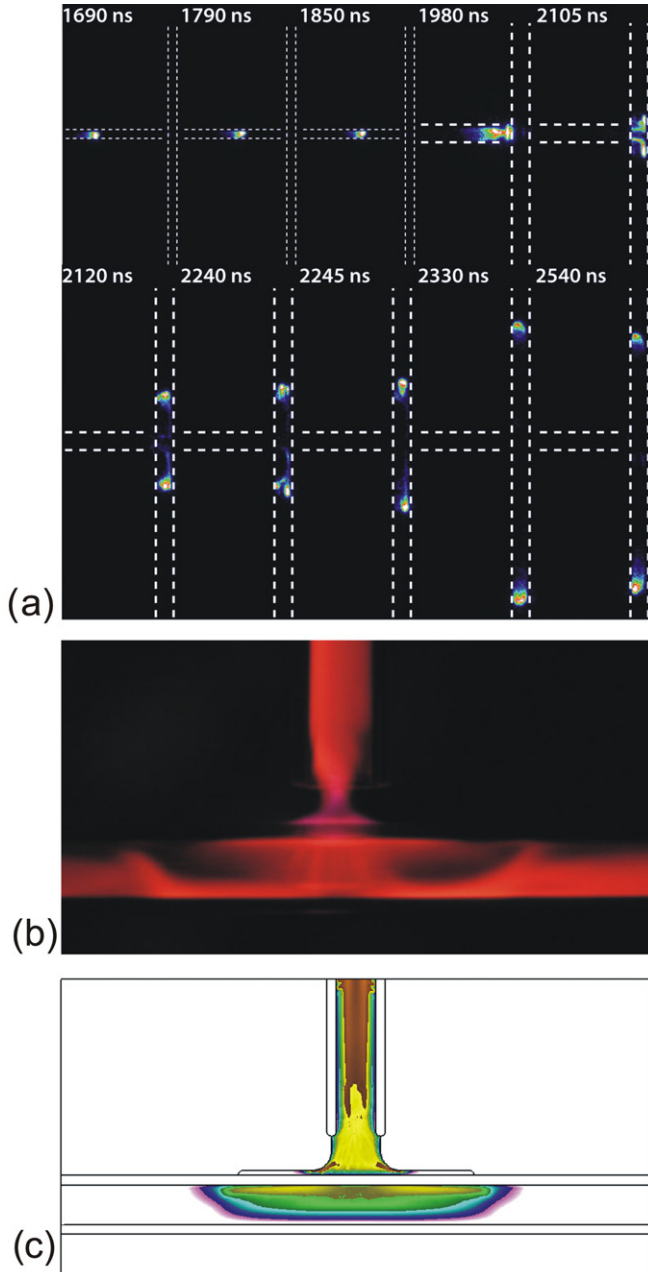
Figure 3. Experimental images of atmospheric-pressure plasma transfer with positive polarity. (*a*) time-resolved (10 ns exposure) showing the sequence of ionization front propagating between the source and transfer tubes with microsecond voltage pulse. (25 kV Gaussian pulse, FWHM ≈ 4 μs). (*b*) Time-integrated (160 ms exposure) neon emission showing the penetration of the primary IW through the dielectric wall and the generation of secondary IWs inside the transfer tube. (*c*) Time-integrated density of Ne excited states in the simulation representing the source of optical emission.

are also observed crossing the transfer tube underneath the source tube. This may be a result of the (earlier) propagation of the secondary IWs towards the opposite wall. Overall, the most intense emission in the transfer tube occurs when the two secondary IWs propagate away from the intersection with the source tube.

The plasma transfer process for the negative primary IW, driven by either microsecond or nanosecond voltage pulses as shown in figures 4(*a*) and (*b*), is distinctively different
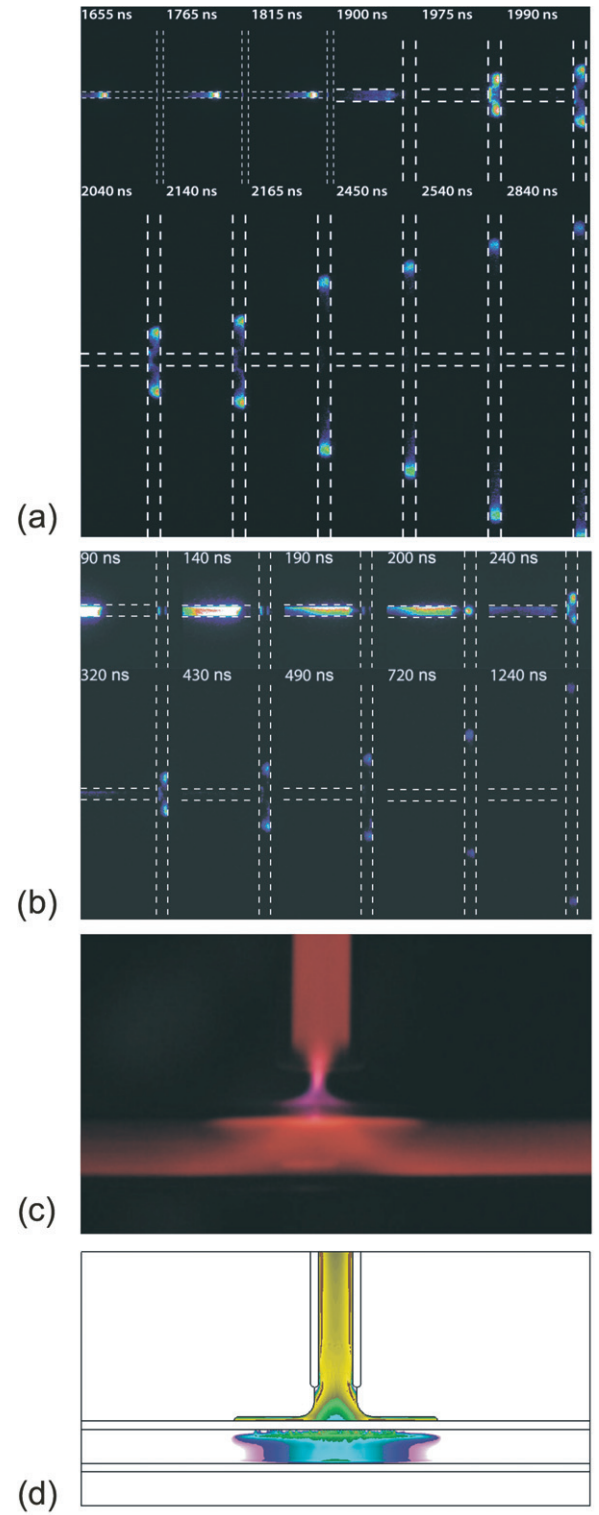
Figure 4. Experimental images of atmospheric-pressure plasma transfer with negative polarity. (*a*) time-resolved (10 ns exposure) showing the sequence of ionization front propagating between the source and transfer tubes with microsecond voltage pulse (−25 kV Gaussian pulse, FWHM ≈ 4 μs). (*b*) Time-resolved (10 ns exposure) showing the sequence of ionization front propagating between the source and transfer tubes with nanosecond voltage pulse (−25 kV, ≈50 ns rise time and 1 μs pulse length). (*c*) Time-integrated (160 ms exposure) neon emission showing the formation of the surface charge layer at the top inner surface prior to the generation of the secondary IWs in the transfer tube. (*d*) Time-integrated density of Ne excited states in the simulation representing the source of optical emission.
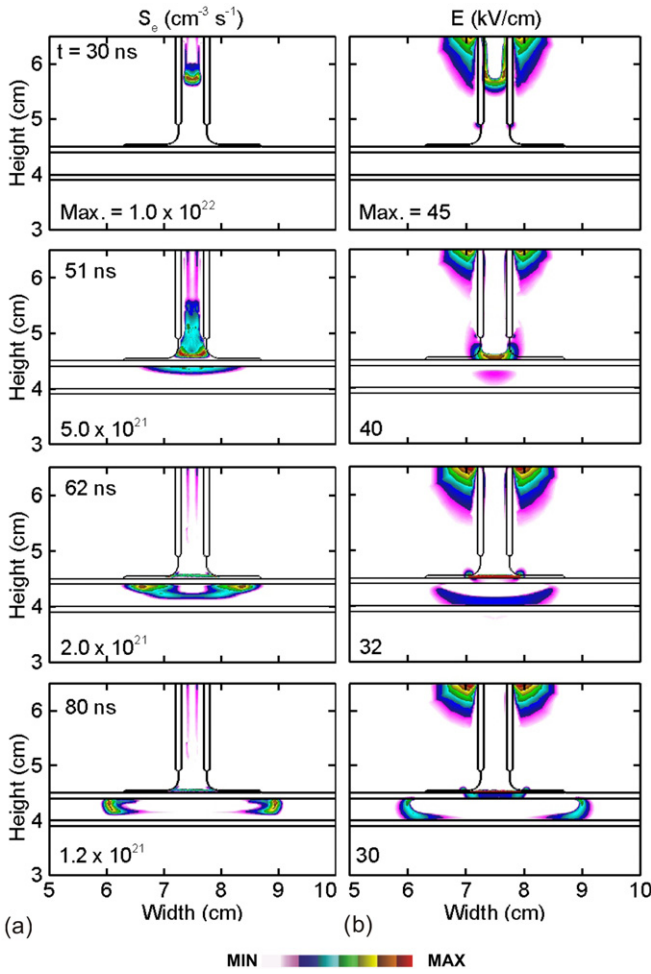
Figure 5. The impingement and penetration of the positive primary IW and the initiation and development of the secondary IWs between $t = 30$ and 80 ns. (*a*) Electron impact ionization rate S_e. (*b*) Electric field. Contours are on a log scale over 4 decades.

Figure 6. The impingement and penetration of the positive primary IW and the initiation and development of the secondary IWs between $t = 30$ and 80 ns. (*a*) Electron density n_e. (*b*) Electron temperature T_e and electric potential shown as line contours. Contours for n_e are on a log scale over 4 decades.

from its positive counterpart. Integrated optical emission from the microsecond driving pulse is shown in figure 4(*c*). The propagation of the primary IW through and out of the source tube is similar to the positive case—the IW impinges on the outer surface of the transfer tube, presumably charging it negatively. However in the negative case, there is strong emission along the inner wall of the transfer tube underneath where the primary IW impinges. This layer is best seen in the images between 1975 and 2140 ns in figure 4(*a*), between 240 and 430 ns in figure 4(*b*) and in the time-integrated emission. For the nanosecond voltage pulse, early initiation of the secondary IW produced by the impinging primary IW is captured by the bright emission dot inside the transfer tube at $t = 200$ ns, as shown in figure 4(*b*). Emanating from the wall-hugging emission of the secondary IW are filaments of bright emission ending on the opposite wall. The secondary IWs then propagate in opposite directions, at first wall hugging along the far wall and later evolving into an IWs centred on axis.

3.2. Computed characteristics of the positive primary IW

The sequence of plasma transfer for the positive primary IW is shown in figures 5 and 6, including the propagation in the
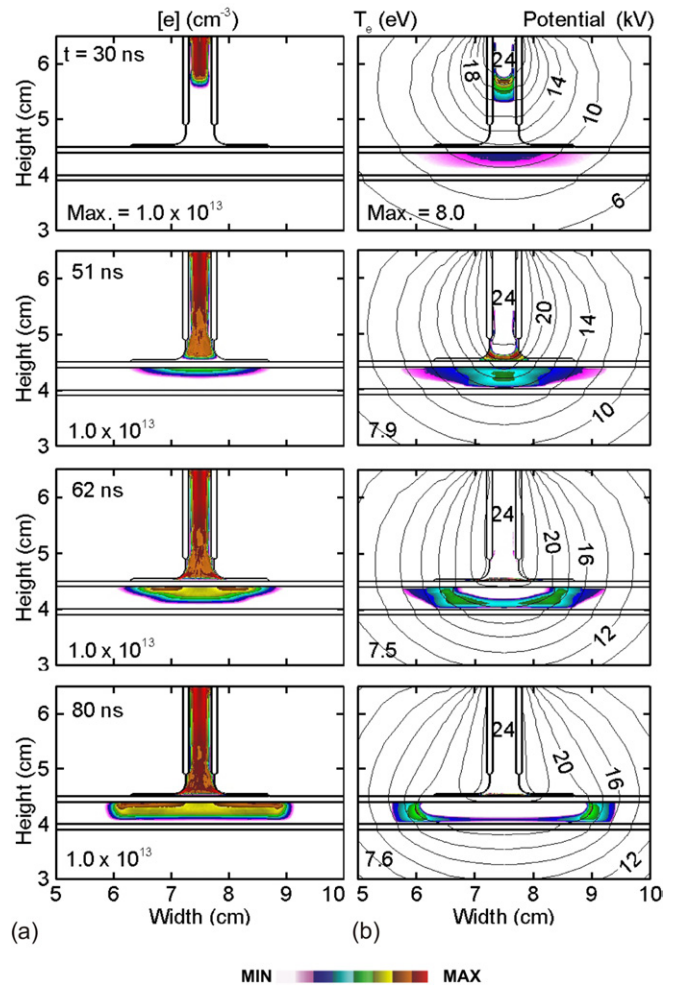
source channel, the apparent penetration through the dielectric wall and the generation of two secondary IWs in the transfer channel. The ionization front, represented by the rate of electron impact ionization, S_e (cm^3 s^{-1}), and the total electric field E at the times of $t = 30$, 51, 62 and 80 ns after the initiation of the discharge, are shown in figure 5. The electron density, electron temperature T_e and electric potential contours are shown in figure 6. S_e typically reaches its maximum in the head of the avalanche where the E is the largest (within the plasma) due to space charge separation. The positive primary IW approaches the inter-channel space (30 ns), with a speed v_p, about 7×10^7 cm s^{-1}, and impinges on the upper surface of the top transfer channel wall (51 ns). The primary IW then spreads into the thin layer on top of the transfer channel which has the large mole fraction of Ne where it continues to propagate laterally. The IW then appears to penetrate the transfer channel and produce two laterally propagating IWs. This results from at least two effects.

As a result of the impingement of the IW on the top of the transfer channel and spreading on the surface, the top surface is charged positively. This occurs at a time when a

J. Phys. D: Appl. Phys. **46** (2013) 155203

Z Xiong *et al*

conductive plasma channel is completed from the anode to the top of the transfer channel. This effectively transfers the anode potential (minus about 1 kV voltage drop along the plasma) to the surface of the transfer channel. About 2 kV is dropped across the top wall of the transfer channel. The electric field appearing at the top of the plasma channel is approximately 30 kV cm^{-1} (120 Td) which, combined with a small residual background density, produces a downward directed electron avalanche under the top surface of the channel. By $t = 62$ ns, this avalanche has reached the lower inner surface of the transfer channel which fills the channel with conductive plasma and charges the lower surface. Lateral components of the electric field pointing left-and-right from the intersection point are produced. At $t = 80$ ns, the surface IW fronts eventually develop into two positive secondary IWs filling a large part of the channel width and propagating at a speed of $v_s = 3 \times 10^7$ cm s^{-1}. The plasma does not uniformly fill the transfer channel, as the plasma retains a top surface-hugging mode. The electron density in the top primary channel is $n_e = 3 \times 10^{12}$ cm^{-3} and in the lower transfer tube is 2×10^{10} cm^{-3}, which produces a more resistive plasma having a somewhat slower IW speed.

The characteristics of this top-to-bottom avalanche process are also reflected in the distribution of the electron density n_e and electron temperature T_e, as shown in figure 6. The IWs in the transfer channel start from the top surface ($t = 51$ ns), and the electron density near the top wall is higher than that near the bottom wall. At $t = 80$ ns the peak n_e in the plasma channel basically hugs the top inner surface. The evolution of T_e nearly follows that of the electric field. Well before the primary IW penetrates the top dielectric wall ($t = 30$, 51 ns), the seed electrons in the transfer channel have already been heated by the approaching electric field to about 6 eV.

The distribution of S_e and the electric field in the transfer channel have an inverted D shape, which closely resembles the time-integrated experimental optical emission shown in figure 3(*b*). To approximate the experimentally derived time-integrated optical emission, we integrated over the duration of our simulation the density of Ne excited states which would be the source of optical emission. This time integration, shown in figure 3(*c*), closely resembles that of the experiment. In short, the positive polarity plasma transfer results from penetration of the electric field and transfer of positive potential through the conductive plasma channel by the impingement the primary IW onto the top of the transfer channel. Within the transfer channel, the generation of the secondary IWs is basically a *top-down* process. That is, the IW starts from the top inner surface and extends to the bottom inner surface before eventually developing into side-travelling ionization fronts. Similar to the primary IW in the source channel, the lateral propagating secondary IWs are also positive.

These simulations were performed with a maximum preionization density $[e] \approx 10^8$ cm^{-3} in the transfer tube. At least for the first pulse, there is no clear mechanism for the IW to produce seed electrons by, for example, photoionization as the wall of the channel will not transmit ionizing radiation from the primary IW. The magnitude of the electric field across
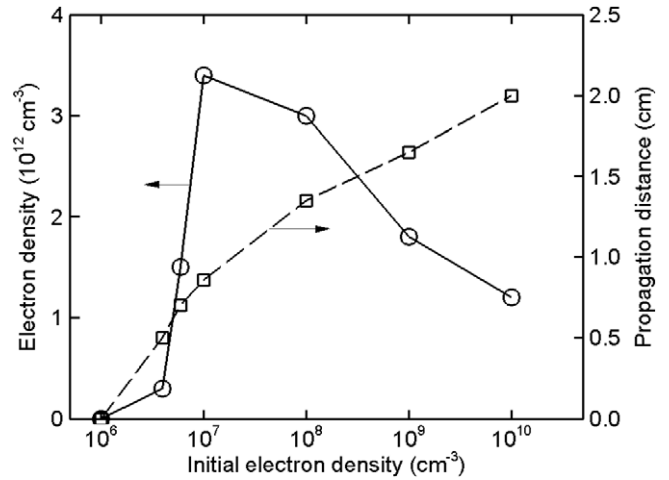

Figure 7. The peak electron density and propagation distance of the secondary IWs at $t = 75$ ns as a function of the preionization density level in the transfer channel for positive primary IW.

the channel wall is insufficient to produce electrons by field emission from the wall. In multiply pulsed discharges, even at low repetition rates, there will be some residual electron density to seed the avalanche. There is the possibility that visible radiation produced by the primary IW would photo-detach residual electrons on the inner surface of the transfer tube left over from a previous pulse. This would give the appearance of photoionization. Pechereau *et al* [17] found in their study of plasma penetration across dielectric barriers that allowing the barrier to be transparent to ionizing radiation decreased ignition times, but otherwise properties of the transferred IW were not particularly affected.

The sensitivity of the transferred IWs to the background preionization density is shown in figure 7 by the peak electron density in the transfer tube and propagation distance of the transferred IWs at $t = 75$ ns (the end of the constant voltage phase). Preionization density levels were varied between 10^6 to 10^{10} cm^{-3}. There is a threshold of the preionization density, $[e] \approx 4 \times 10^6$ cm^{-3}, below which the secondary IWs cannot be ignited during the 75 ns of applied voltage. (Longer waveforms were not investigated.) The production of the IW in the transfer tube requires a critical plasma density to produce sufficient space charge in the head of the IW to initiate avalanche. This density is approximately 10^{10} cm^{-3}. Beginning at lower preionization densities requires longer avalanche (and avalanche distances) to achieve this density. Preionization densities of 10^6 cm^{-3} or lower have avalanche times or distances that are too long to achieve this density during the pulse width and channel width of the experiment.

Once ignited, the dynamics of the secondary IWs are relatively insensitive to the level of preionization. For the preionization density increasing from 3×10^6 to 10^7 cm^{-3}, the peak electron density of the secondary IWs at $t = 75$ ns increases to 3.5×10^{12} cm^{-3}. Further increasing the preionization density to 10^{10} cm^{-3} decreases the peak electron density in the IW to 1.2×10^{12} cm^{-3}. The distance that the secondary IW wave travels during the first 75 ns monotonically increases to 2.0 cm as the preionization density increases. This is more a consequence of an increase in the speed of
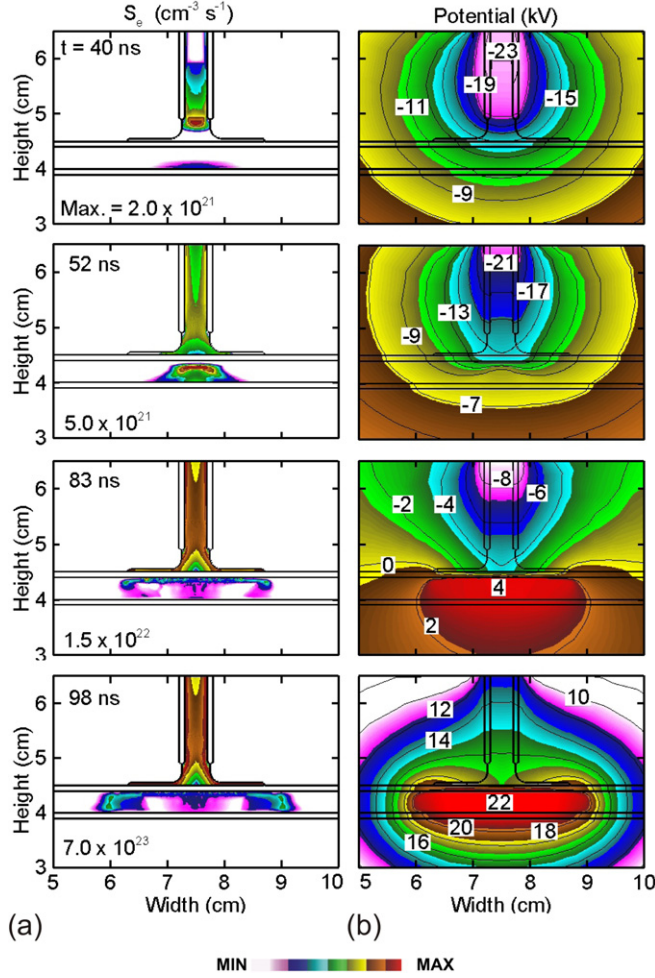
J. Phys. D: Appl. Phys. **46** (2013) 155203

Z Xiong *et al*

Figure 8. The impingement and penetration of the negative primary IW and the initiation and development of the secondary IWs between $t = 40$ and 98 ns. (*a*) Electron impact ionization rate S_e. (*b*) Electric potential. Contours for S_e are on a log scale over 4 decades.
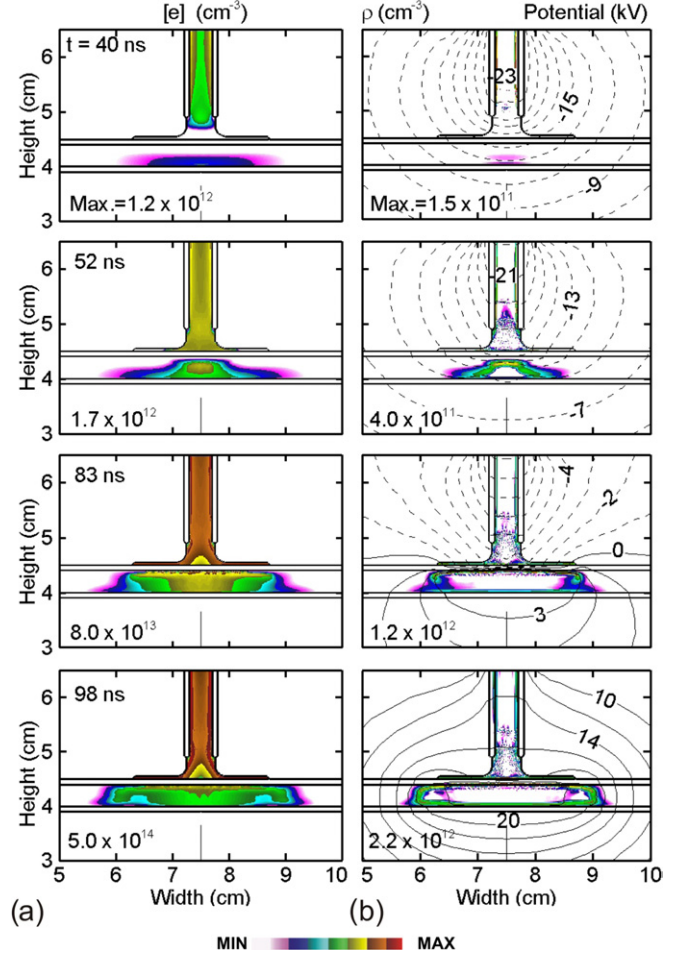

Figure 9. The impingement and penetration of the negative primary IW and the initiation and development of the secondary IWs between $t = 40$ and 98 ns. (*a*) Electron density n_e (*b*) Net space charge ρ and electric potential. Contours for n_e and ρ are on a log scale over 4 decades. The negative and positive potential are shown by the dashed and solid contour lines, respectively.

the IW than a delay in launching of the secondary IW as the preionization density decreases. The speed of the IW increases from $2.5 \times 10^7 \, \text{cm s}^{-1}$ to $1.0 \times 10^8 \, \text{cm s}^{-1}$ as the preionization density increases from 10^6 to $10^{10} \, \text{cm}^{-3}$. This effect is similar to a conventional streamer propagating into a preionized gas—the speed of the streamer increases with increasing preionization density.

3.3. Computed characteristics of the negative primary IW

The sequence of plasma transfer for the negative primary IW is shown in figure 8 by the electron impact ionization rate S_e and the electric potential at $t = 40, 52, 83$ and 98 ns after the discharge initiation. The electron density, charge density and electric potentials are shown in figure 9. Similar to the positive case, the plasma transfer process for the negative primary IW consists of propagation in the source channel, crossing the gap between the channels and the impingement of the IW upon the top surface of the transfer channel. Two secondary, counter-propagating IWs are similarly produced in the transfer channel. The speed of the primary IW, $v_p \approx 6 \times 10^7 \, \text{cm s}^{-1}$,

is slightly lower than that for the positive IW for otherwise the same conditions. The speeds of the secondary IWs, around $3 \times 10^7 \, \text{cm s}^{-1}$, are also slightly lower than the positive case. However, there are two important differences in the transfer dynamics between the negative and positive primary IWs.

The first difference lies in how the secondary IWs in the transfer channel are produced. Unlike the top-down process described for the positive case, the production of the secondary IWs for negative case is a *bottom-up* process. That is, avalanche in the transfer channel starts from the bottom wall and propagates to the top wall. When the negative primary IW first approaches the inter-channel gap ($t = 40$ ns), there is electric field penetration through top wall of the transfer channel, which accelerates the preionization electrons downwards, accumulating near and charging the lower surface. As the primary IW impinges upon and then spreads along the top wall ($t = 52$ ns), a conducting channel is formed, through which the negative potential of the cathode is nearly transferred to the top surface of the transfer channel and charges it negatively. Meanwhile, an ionization front first initiates from the high electron density region near the bottom wall, and then

develops into an avalanche with a convex front propagating towards the top wall.

When the negative primary IW impinges on the top wall and transfers the cathode potential, the top surface becomes a temporary cathode. The bottom wall of the transfer channel however remains at a floating potential and thus serves as a temporary anode. The upwardly moving discharge induced in the transfer channel is at this point essentially a positive, cathode-bound streamer. When this IW impinges upon the top inner surface, a positive surface charge is produced, as shown in figure 9. The highest ionization source S_e at this point ($t = 83$ ns) is adjacent to the positive surface charge layer. This initiation process for the secondary IW agrees well with the emission images in figures 4(*a*) and (*b*). Particularly for the nanosecond voltage pulse, the formation of the positive, left-travelling streamer and its ensuing impingement upon the tube surface are clearly captured between 200 and 240 ns. The bottom-up development of the curved avalanche front and the formation of the horizontal surface charge layer also explain, in part, the time-integrated optical emission shown in figure 4(*c*). The strong plasma emission layer near the top inner surface of the transfer tube results from the intense electric field (40 kV cm^{-1}, 160 Td) adjacent to the positive surface charge layer. The continuing accumulation of the positive surface charge produces lateral components of the electric field which launch IWs to the left and right. At $t = 98$ ns, the bottom-up transfer process has basically completed, with two secondary IWs having wall-hugging S_e propagating in opposite directions in the transfer channel.

The second major difference between the negative and positive primary IW case is a reversal of polarity of the secondary IWs produced by the negative primary IW. The upper wall of the transfer channel acts as a capacitor whose top surface is charged to the negative potential of the cathode, brought by the conductive plasma in the primary channel. The positive, upward directed avalanche in the transfer channel deposits positive charge on the inner surface of the transfer channel wall to counter balance the charge on the top surface of this capacitance. However, the values of potential at this point remain negative within the entire domain. As this positive charge accumulates, the local potential reverses its polarity, from 4 kV at $t = 83$ ns directly underneath the impingement zone, to as high as 22 kV at $t = 98$ ns. Since the ends of the transfer tube are at a floating potential (with ground 3–4 cm further away), a positive electric field is produced pointing from the positive surface charge layer (and positive potential) towards the ends of the transfer channel. When the electric field reaches 20 kV cm^{-1} (80 Td), IWs are launched in either direction. At this point, the two secondary IWs in the transfer channel are in fact driven by a *positive* potential.

The bottom-up IW generation process and polarity reversal for the secondary IWs are further illustrated by the electron density n_e and net space charge ρ in figure 9. The initial concentration of n_e near the bottom wall, 9×10^9 cm^{-3}, at $t = 40$ ns results from the penetrating electric field of the approaching primary IW, which at this point is just exiting the source channel. At $t = 52$ ns, a positive avalanche has occurred in the transfer channel, increasing n_e to 3×10^{12} cm^{-3}.
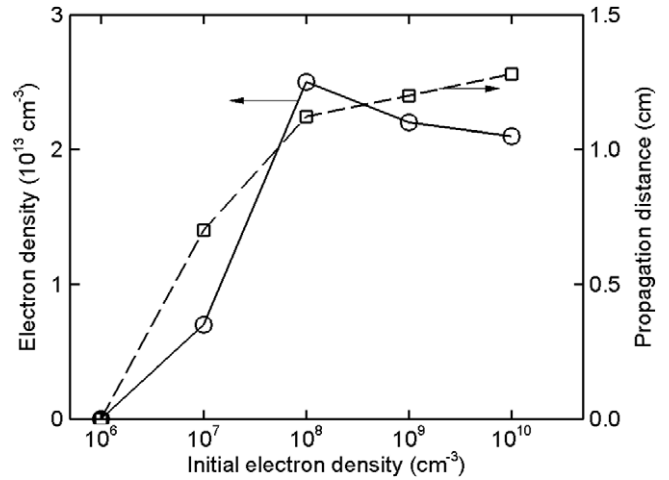

Figure 10. The peak electron density and propagation distance of the secondary IWs at $t = 75$ ns as a function of the preionization density level in the transfer channel for negative primary IW.

When the positive streamer reaches the top wall, the plasma region spreads laterally along its inner surface while the primary IW does the same along its outer surface ($t = 83$ ns). The further development of the two secondary IWs then starts to fill the channel as they propagate sideways. The positive space charge ρ is also an indication of the location of the ionization front and of the surface charging. At 40 ns, a small positive space charge, 3×10^9 cm^{-3}, near the lower surface of the transfer channel indicates the start of an IW moving upwards. The arrival of the IW at the top surface ($t = 52$ ns) and its lateral propagation ($t = 83$ ns) indicate the positive nature of the outward moving IWs.

Again, to approximate the experimentally derived time-integrated optical emission, we integrated over the duration of our simulation the density of Ne excited states which would be the source of optical emission. This time integration, shown in figure 4(*d*), also closely resembles that of the experiment.

Note that upon arrival of the upwards travelling IW in the transfer tube, the ionization rate in the primary tube increases and there is a small increase in electron density. A small upward moving positive space charge wave in the primary tube indicates a re-strike wave, now positive, that propagates back to the cathode.

In short, the negative polarity plasma transfer results from negative charging of the top surface of the transfer channel, and production of positive space charge on the inner surface of the transfer channel that reverses polarity. Within the transfer channel, the generation of the secondary IWs is basically a *bottom-up* process. That is, the IW starts from the bottom surface of the transfer channel and extends to the top surface before eventually developing side-travelling IWs.

As with the positive polarity case, these simulations were performed with a peak preionization density in the transfer channel of $[e] \approx 10^8$ cm^{-3}. The sensitivity of the transferred IWs to the background preionization for the negative primary IW is shown in figure 10. The peak electron density and the propagation distance of the transferred IWs at $t = 75$ ns are plotted for preionization levels varying from 10^6 to 10^{10} cm^{-3}. Similar to the positive case, there is a threshold of preionization
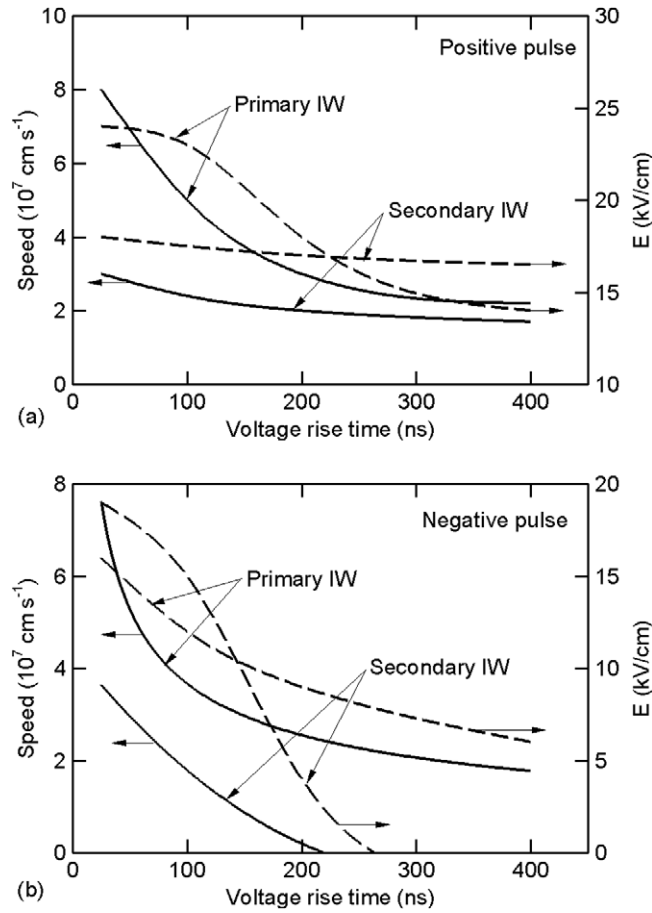
Figure 11. The speeds and electric fields of the primary and secondary IWs as a function of the voltage rise time for (*a*) positive and (*b*) negative voltage pulses. The speeds and electric fields are computed at the exit of the source channel for the primary IW and 1.5 cm away from the centre line for the secondary IWs.

density, $[e] \approx 10^6$ to $10^7 \, cm^{-3}$ for the secondary IWs to be ignited by the impinging negative primary IW during the applied voltage pulse. The peak plasma density in the transfer tube, $2.5 \times 10^{13} \, cm^{-3}$, is larger than for the positive case, and occurs at a higher preionization density ($10^8 \, cm^{-3}$). However as with the positive IW case, once ignited, the dynamics of the secondary IWs are essentially independent of the preionization levels in the transfer channel.

3.4. Effects of the voltage rise time

In addition to polarity, the intensity of the primary IWs (e.g., speed of the IW, plasma density in the head of the IW) also affects the plasma transfer process. To a certain degree, the intensity of an IW depends on the rise time of the voltage pulse that generates it—shorter rise times produce more intense IWs. To investigate these issues, the time of the voltage pulse to increase linearly from 0 to ± 25 kV was varied from 25 to 400 ns in the model. After reaching its peak value, the voltage was kept constant for 50 ns before linearly decreasing to zero over the same rise time period. The speeds and peak electric fields of the primary and secondary IWs as a function of the voltage rise time are shown in figure 11. The speeds for the

primary IW were measured at the exit of the source channel where the IW enters the inter-channel gap. The speeds of the secondary IWs in the transfer channel were measured 1.5 cm on either side of the centre line.

For the positive primary IW, the transfer processes for different rise times are qualitatively similar. With increasing voltage rise time the primary IW speed decreases, as does its peak electric field. The wave speed decreases from $8 \times 10^7 \, cm \, s^{-1}$ for a rise time of 25 ns to $2.3 \times 10^7 \, cm \, s^{-1}$ for a rise time of 400 ns, and the peak electric field decreases from $23 \, kV \, cm^{-1}$ (92 Td) to $14 \, kV \, cm^{-1}$ (56 Td). Concurrently, the speed of the secondary IWs, produced by the penetrating primary IW, also decreases—from $3 \times 10^7 \, cm \, s^{-1}$ to $1.8 \times 10^7 \, cm \, s^{-1}$. The speed of the primary wave depends upon the rise time more sensitively than that of secondary IWs.

With a negative polarity, the general dependences of wave speed and electric field on voltage rise are similar to the positive case—increasing rise time produces decreasing IW speeds and reduced electric fields. However, both the speed and the electric field of the secondary IW decrease faster than those of the primary IW as the rise time increases. There is finally a voltage rise time beyond which the secondary IWs cannot be produced. For these cases, the threshold is about 220 ns, corresponding to the point where the speed of secondary IWs goes to zero. This may be explained by an equivalent dielectric relaxation time for the lumped system consisting of dielectric transfer channel and the plasma within. As discussed above, the generation of secondary IWs by a negative primary IW is a bottom-up process. This bottom-up process requires the formation of a cathode-bound streamer which can only be initiated when there is a large enough electric field, or equivalently potential difference, between the top and bottom walls of the transfer channel.

Since the potentials at both the top and bottom walls of the transfer tube are floating, a slowly varying potential field introduced by the primary IW compared to the dielectric relaxation time will tend to smooth the potential distribution and reduce the electric field in the transfer tube. To produce the required potential difference to launch the secondary IW, the primary IW needs to deposit a critically large amount of charge at a sufficiently high rate on the top of the transfer channel. In such cases, the top wall becomes a temporary cathode, while the bottom wall, a temporary anode. The large electric field then initiates the streamer discharge which then forms the surface positive layer near the top wall and eventually develops into the two secondary IWs.

We note that these simulations address impingement of only one single primary IW. In the experiments, the plasma source is often operated at repetition rates where there may be charge remaining on the outer surface of the transfer tube from prior pulses. This charge may aid in producing secondary IWs on successive pulses even with a relatively long rise time of the applied voltage pulses. We believe this is the main reason for the successful ignition of secondary IWs in the experiments even with microsecond voltage pulses as shown in figure 4(*a*). Another reason could be due to the geometric difference between the tubes used in the experiments and the channels used in the simulation. In the experiments, the plasma

J. Phys. D: Appl. Phys. **46** (2013) 155203

Z Xiong *et al*

layer formed on the outer surface of the transfer tube develops in both axial and circumferential directions, i.e. it hugs the transfer tube at the impingement zone. This would induce a stronger and more focused 3D electric field in the transfer tube than those in a planar channel in the simulations. In the latter case, the plasma layer can only develop on the top channel wall and only along the axial direction.

4. Concluding remarks

Plasma transfer refers the phenomenon that a primary IW produced in a source tube is capable of generating a secondary IW in a spatially separated and electrodeless tube by impinging upon its outer surface. Two-dimensional numerical simulations and experiments were performed of plasma transfer across dielectric channels and tubes. The source and transfer channels are placed perpendicularly to each other in ambient air with a 4 mm gap. Both channels are filled with Ne or Ne/Xe mixtures (99.9/0.1) at atmospheric pressure and at room temperature. Plasma transfer initiated by both positive and negative voltage pulses were investigated, and the predicted transfer dynamics were found to qualitatively agree with the experimental observations. For the positive primary IW, the transfer is a top-down process, characterized by the penetration of the high electric field at the primary IW front through the dielectric wall of the transfer channel. The secondary IWs generated in the transfer channel have the same positive polarity as the primary IW.

For the negative primary IW, however, the plasma transfer is a bottom-up process, mediated by a streamer discharge propagating across the transfer channel from the bottom to the top wall. The streamer discharge is induced by the deposition of the electrons on the outer surface of the transfer channel wall. Upon impinging the top wall, the streamer produces a strong positive surface charge layer on its inner surface. As a result, large positive potentials emerge from the transfer channel which counter balance the incoming (negative) IW potential and initiate the two secondary IWs in the transfer channel. The polarity of the two secondary IWs is reversed from that of the negative primary IW. A threshold preionization density in the transfer channel, $[e] \approx 10^6–10^7\ \mathrm{cm}^{-3}$, is found to be necessary for the secondary IWs to be ignited. Once ignited, however, the dynamics of the secondary IWs only weakly depend on the preionization level. The speeds of the primary and secondary IWs are found to depend on the voltage rise time. Increasing rise time decreases the speeds of both primary and secondary IWs. While the plasma transfer process for positive polarity at different rise time are similar, there exists a threshold rise time for negative polarity, beyond which the secondary IWs cannot be generated by a single negative primary IW.

Acknowledgments

References

[1] Starikovskaia S M, Anikin N B, Pancheshnyi S V, Zatsepin D V and Starikovskii A Y 2001 Pulsed breakdown at high overvoltage: development, propagation and energy branching *Plasma Sources Sci. Technol.* **10** 344

[2] Adamovich I V, Choi I, Jiang N, Kim J-H, Keshav S, Lempert W R, Mintusov E, Nishihara M, Samimy M and Uddi M 2009 Plasma assisted ignition and high-speed flow control: non-thermal and thermal effects *Plasma Sources Sci. Technol.* **18** 034018

[3] Pothiraja R, Bibinov N and Awakowicz P 2011 Amorphous carbon film deposition on the inner surface of tubes using atmospheric pressure pulsed filamentary plasma source *J. Phys. D: Appl. Phys.* **44** 355206

[4] Laroussi M 2002 Nonthermal decontamination of biological media by atmospheric-pressure plasmas: review, analysis, and prospects *Trans. Plasma Sci.* **30** 1409

[5] Stoffels E, Sakiyama Y and Graves D 2008 Cold atmospheric plasma: charged species and their interactions with cells and tissues *Trans. Plasma Sci.* **36** 1441

[6] Fridman G, Friedman G, Gutsol A, Shekhter A B, Vasilets V N and Fridman A 2008 Applied plasma medicine *Plasma Proc. Polym.* **5** 503

[7] Kong M G, Kroesen G, Morfill G, Nosenko T, Shimizu T, van Dijk J and Zimmermann J L 2009 Plasma medicine: an introductory review *New J. Phys.* **11** 115012

[8] Kim J Y, Kim S, Wei Y and Li J 2010 A flexible cold microplasma jet using biocompatible dielectric tubes for cancer therapy *Appl. Phys. Lett.* **96** 203701

[9] Robert E, Sarron V, Riès D, Dozias S, Vandamme M and Pouvesle J-M 2012 Characterization of pulsed atmospheric-pressure plasma streams (PAPS) generated by a plasma gun *Plasma Sources Sci. Technol.* **21** 034017

[10] Jánský J, Le Delliou P, Tholin F, Tardiveau P, Bourdon A and Pasquiers S 2011 Experimental and numerical study of the propagation of a discharge in a capillary tube in air at atmospheric pressure *J. Phys. D: Appl. Phys.* **44** 335201

[11] Mrad O, Saunier J, Aymes Chodur C, Rosilio V, Agnely F, Aubert P, Vigneron J, Etcheberry A and Yagoubi N 2010 A comparison of plasma and electron beam-sterilization of PU catheters *Radiat. Phys. Chem.* **79** 93

[12] Hoffmann M, Bruch H, Kujath P and Limmer S 2010 Cold-plasma coagulation in the treatment of malignant pleural mesothelioma: results of a combined approach *Interact Cardio-Vasc. Thorac. Surg.* **10** 502

[13] Robert E, Vandamme M, Sobilo J, Sarron V, Riès D, Dozias S, Brulle L, Lerondel S, Le Pape A and Pouvesle J M 2012 First achievements and opportunities for cancer treatment using non thermal plasma *Plasma for Bio-Decontamination, Medicine and Food Security (NATO Science for Peace and Security Series A: Chemistry and Biology)* ed Z Machala *et al* (Eindhoven: Springer)

[14] Sarron V, Robert E, Dozias S, Vandamme M, Ries D and Pouvesle J M 2011 Splitting and mixing of high-velocity ionization-wave-sustained atmospheric-pressure plasmas generated with a plasma gun *Trans. Plasma Sci.* **39** 2356

[15] Xiong Z and Kushner M J 2012 Atmospheric pressure ionization waves propagating through a flexible high aspect ratio capillary channel and impinging upon a target *Plasma Sources Sci. Technol.* **21** 034001

[16] Xiong Z, Robert E, Sarron V, Pouvesle J-M and Kushner M J 2012 Dynamics of ionization wave splitting and merging of atmospheric-pressure plasmas in branched dielectric tubes and channels *J. Phys. D: Appl. Phys.* **45** 275201

[17] Pechereau F, Jánský J and Bourdon A 2012 Simulation of the reignition of a discharge behind a dielectric layer in air at the atmospheric pressure *Plasma Sources Sci. Technol.* **21** 055011

[18] Lu X *et al* 2009 Propagation of an atmospheric pressure plasma plume *J. Appl. Phys.* **105** 043304

[19] Wu S, Wang Z, Huang Q, Xiong Q and Lu X 2011 Plasma plume ignited by plasma plume at atmospheric pressure *Trans. Plasma Sci.* **39** 2292

[20] Johnson V S, Zhu W, Wang R, Re J L, Sivaram S, Mohoney J and Lopez J L 2011 A cold atmospheric-pressure helium plasma generated in flexible tubing *Trans. Plasma Sci.* **39** 2360

[21] O'Connell D *et al Plasma Sources Sci. Technol.* submitted

[22] Karakas E, Koklu M and Laroussi M 2010 Correlation between helium mole fraction and plasma bullet propagation in low temperature plasma jets *J. Phys. D: Appl. Phys.* **43** 155202

[23] Xiong R, Xiong Q, Nikiforov A Y, Vanraes P and Leys C 2012 Influence of helium mole fraction distribution on the properties of cold atmospheric pressure helium plasma jets *J. Appl. Phys.* **112** 033305